Distribution of Mid-Latitude Ground Ice on Mars from New Impact Craters
Shane Byrne, *et al.*
Science **325**, 1674 (2009);
DOI: 10.1126/science.1175307

Distribution of Mid-Latitude Ground Ice on Mars from New Impact Craters

Shane Byrne,[1*] Colin M. Dundas,[1] Megan R. Kennedy,[2] Michael T. Mellon,[3] Alfred S. McEwen,[1] Selby C. Cull,[4] Ingrid J. Daubar,[1] David E. Shean,[2] Kimberly D. Seelos,[5] Scott L. Murchie,[5] Bruce A. Cantor,[2] Raymond E. Arvidson,[4] Kenneth S. Edgett,[2] Andreas Reufer,[6] Nicolas Thomas,[6] Tanya N. Harrison,[2] Liliya V. Posiolova,[2] Frank P. Seelos[5]

New impact craters at five sites in the martian mid-latitudes excavated material from depths of decimeters that has a brightness and color indicative of water ice. Near-infrared spectra of the largest example confirm this composition, and repeated imaging showed fading over several months, as expected for sublimating ice. Thermal models of one site show that millimeters of sublimation occurred during this fading period, indicating clean ice rather than ice in soil pores. Our derived ice-table depths are consistent with models using higher long-term average atmospheric water vapor content than present values. Craters at most of these sites may have excavated completely through this clean ice, probing the ice table to previously unsampled depths of meters and revealing substantial heterogeneity in the vertical distribution of the ice itself.

Using theoretical models, previous investigators predicted that buried water ice is stable at high latitudes on Mars beneath a desiccated soil layer (*1*–*4*) with an extent and depth that depend on temperature and humidity (which vary with changing orbital elements). Hydrogen abundances inferred from gamma-ray, high-energy neutron and neutron spectrometer (NS) data show that the uppermost decimeters of the martian surface contain large amounts of water ice poleward of latitudes ±60° (*5*–*8*), which can exceed 50% by mass (~75% by volume). A key parameter setting the extent of stable ground ice is the global average atmospheric water vapor. Models suggest 20 precipitable micrometers (pr-μm) best explains the NS data (*9*), whereas direct measurements indicate only 14 pr-μm (*10*) or perhaps even lower (*11*). The mid-latitude boundary enclosing the area where buried ice is presently stable is expected to be abrupt (Fig. 1), and its position is sensitive to this long-term global average (higher atmospheric water vapor results in increased ice stability). However, the NS data (Fig. 1) cannot tightly constrain the location of this abrupt edge (*12*), and although the NS can constrain the depth to the top of the high-latitude ice table, it is insensitive to changes in ice concentration a few centimeters below that (*13*).

Here, we report on a method to probe subsurface ice on Mars. Impact craters with meter- to decameter-scale diameters form frequently (*14*). Analysis of Context Camera (*15*) (CTX) images led to the identification of five such impacts (Fig. 1) near the boundary of Utopia and Arcadia Planitia [see the supporting online material (SOM) for details]. Follow-up observations by the High-Resolution Imaging Science Experiment (HiRISE) (*16*) showed the excavated material to have brightness and color indicative of water ice (Figs. 2 and 3). Impact times are constrained by images taken before and after impact (Table 1).

We examined hyperspectral data from the Compact Reconnaissance Imaging Spectrometer for Mars (CRISM) (*17*) covering these sites for spectral signatures of water ice. In general, the bright material imaged by HiRISE occupies only a few percent of a CRISM pixel (18 m across); however, bright material at site 3 was extensive enough to occupy a substantial fraction of several CRISM pixels. Water ice absorption bands were detected over this feature, but not over adjacent terrain (Fig. 3). The other sites do not show spectral evidence of ice, likely due to their small areas (next largest is site 5, occupying ~0.1 CRISM pixels).

Site 1 contains a cluster of small craters of which many have flat floors, indicating excavation to a mechanically stronger material. Icy material appears in two such craters. Site 5 contains a single crater with isolated interior decimeter-scale spots of ice and a larger (4 m by 9 m) exterior icy patch adjacent to the crater's eastern side only (although the crater and its 1-km-long dark rays are symmetric). Aeolian action may have transported ice within the crater over its eastern rim, a direction consistent with nearby wind observations (*18*). Sites 1 and 5 contain well-developed polygons (7 to 8 m across). Sites 2 and 4 occur in the Phlegra Montes, eroded massifs with associated debris-covered aprons. Site 2 (and perhaps sites 1 and 4) occurs on these lobate aprons, once interpreted as ice-rich debris (*19*); however, similar aprons elsewhere are now known to be composed of relatively pure ice (*20*, *21*). Sites 2 and 4 have ice on their interior crater walls and draped over their rims. Site 3, on dark plains, has excavated subsurface ice almost entirely onto its ejecta blanket. We interpret the absence of bright ice on the crater floor at sites 2 to 5 to indicate that these impacts excavated completely through a relatively thin buried bright ice layer. Other, less likely, alternatives include obscuration by dust fallout (which would not concentrate at the crater bottom), saltating particles collecting inside the crater (no dunes or ripples indicates the presence of such particles in this region), fallback of crater ejecta (yet site 3 ejecta is ice-rich and the crater floor is dark), and slumping of regolith from the walls [however, the site 3 regolith layer is thought to be only 12 cm thick (*9*), and no slumping occurred at site 1]. Bright ice on site 1 crater floors indicates excavation to the bright icy layer, but not through it, consistent with derived crater depths (Table 1).

Monitoring by HiRISE (Fig. 2 and fig. S2) has shown changes in the excavated bright material at all sites, consistent with sublimation of water ice. Exposed mid-latitude water ice is expected to sublimate, causing darkening and reddening as debris within the ice accumulates as a soil lag. Figure 2 shows a clear fading and reddening of icy material at site 1 (its bright blue appearance disappeared over 140 to 200 days). To quantify the total sublimation in this interval, we constructed a one-dimensional thermal model (see SOM). We simulated a dry soil layer with underlying ice to establish the pre-impact subsurface temperatures. We then removed the soil layer and followed the ice surface temperature to calculate sublimation. Among many parameters, the most influential were wind speed

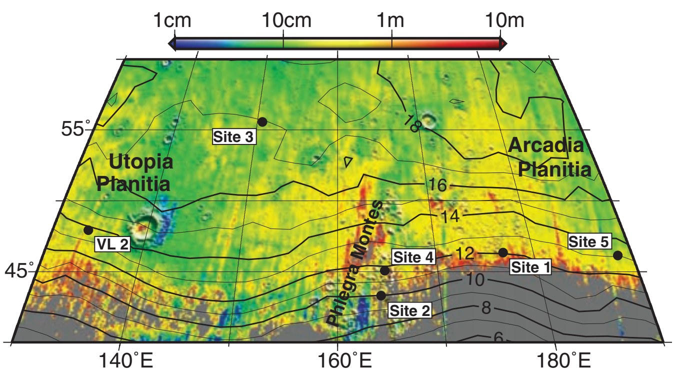

Fig. 1. Expected ice depths (*9*) with Viking Lander 2 and sites 1 to 5 labeled. Contours represent ice depths (g/cm²) derived from NS data. Replotted from data in (*8*).

[1]Lunar and Planetary Laboratory, University of Arizona, Tucson, AZ 85721, USA. [2]Malin Space Science Systems, San Diego, CA 92191, USA. [3]Laboratory for Atmospheric and Space Physics, University of Colorado, Boulder, CO 80303, USA. [4]Department of Earth and Planetary Sciences, Washington University, St. Louis, MO 63130, USA. [5]Applied Physics Laboratory, Johns Hopkins University, Laurel, MD 20723, USA. [6]Physikalisches Institut, Universität Bern, Bern, Switzerland.

*To whom correspondence should be addressed. E-mail: shane@lpl.arizona.edu

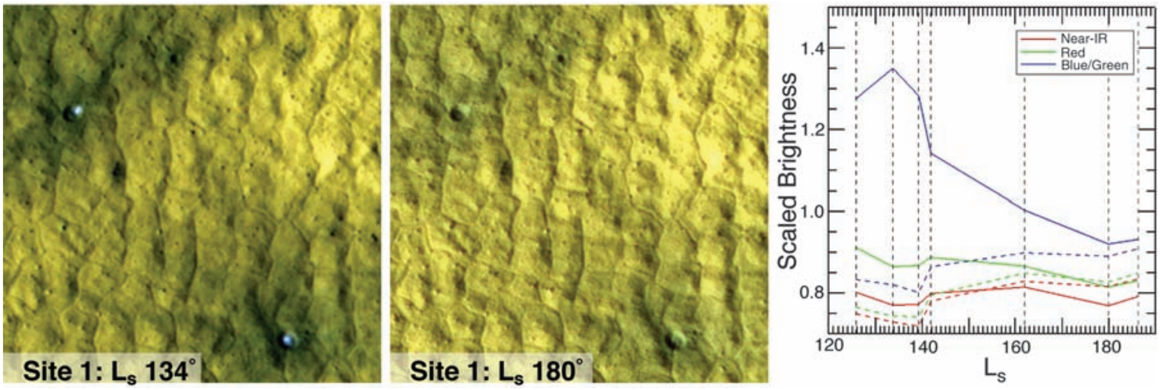

Fig. 2. HiRISE false-color data (see Table 1 for image details) showing sublimation of icy material at site 1. Panels are 75 m across. Images here and in Fig. 3 have north at the top and are illuminated from the lower left. Plot shows the brightness evolution of the lower-right icy patch (solid) and dark impact zone (dashed) in each HiRISE filter scaled by the brightness of the surrounding undisturbed terrain (to remove incidence angle and first-order atmospheric effects). Vertical lines show observation dates. Blue-green and near-infrared bands at L_s 126° were summed 4 × 4.

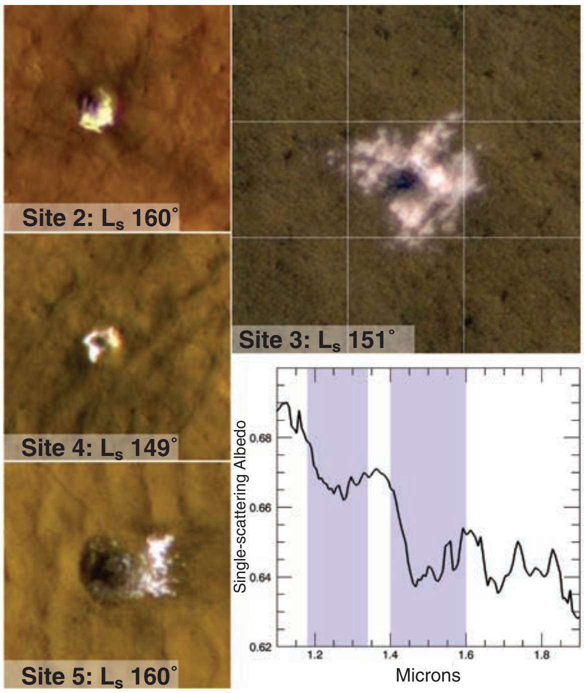

Fig. 3. HiRISE false-color data of sites 2 to 5 (see Table 1 for image details). Left panels are 35 m across; gridlines at site 3 show the scale (18 m) (but not location) of CRISM pixels. CRISM spectrum at lower right with water ice absorption bands indicated is an average of four adjacent pixels in observation FRT0000D2F7.

(nominally 2.5 m s^{-1}) and initial ice albedo (nominally 0.4), which we darkened linearly to background levels by L_s 171°. Varying all parameters within reasonable ranges yielded total sublimations of 0.3 to 6.5 mm, with our nominal case yielding 1.7 mm. Purposefully conservative choices in environmental and physical parameters make this sublimated thickness a robust lower limit (see SOM).

Our estimate of sublimation at site 1 while this ice is fading to background brightness implies clean ice. Experiments indicate that as little as 17 μm of dust masks bright white material at wavelengths of HiRISE's blue-green filter (*16*, *22*). Fading caused by a sublimation lag of dust-sized particles thus implies a debris concentration of only 1% (an upper limit because the sublimation estimate is conservative). The surrounding dark areas (regions blown clear of dust) brighten toward the level of adjacent undisturbed terrain, indicating that atmospheric dust is settling out on the surface. This implies that some of the fading of the ice is caused by this dust fallout rather than by a sublimation lag. Hence, the ice's dust content may be even lower than discussed above. Similarly, if some darkening were caused by ice-grain growth via thermal metamorphism (*23*), then the ice would be even cleaner than derived. Aeolian removal of dust could counter darkening, causing an underestimate of dust content. This is unlikely because brightening of the dark areas indicates dust accumulation. Ice exposed at site 1 is not pore-filling ice, but is relatively pure, at least in the uppermost millimeters. Sites 2, 4, and 5 are at similar latitude and fade at similar rates (fig. S2), implying that this ice is similarly pure. Site 3 (at higher latitude) is fading and shrinking at a slower rate, as expected. It is unlikely that these small impacts can clean ground ice by melting, because melt should easily drain through the ejecta blanket or heavily fractured crater floor.

These craters formed near the abrupt transition from where ground ice is expected to be stable to where it is not (Fig. 1). Here, the expected depth to ice in models is very sensitive to latitude (fig. S4), and its presence in these shallow craters provides a strong test of these models. Results of models using 20 pr-μm of atmospheric water vapor (*9*) agree very well (Table 1) with our data (whereas ground ice at these sites is not expected with 10 pr-μm). Two craters at site 1 appear to have exposed the top of the ice table, and their depths coincide closely with the expected ice-table depth. Sites 2 to 5 have crater depths exceeding the model-predicted depth to ground ice; excavation of ice here is consistent with model results (depth could not be measured for site 3; however, 8-m craters excavate >12 cm). The Phoenix lander encountered both ice-cemented soil and clean ice at 68°N, 234°E (*24*) at depths close to model predictions (*25*). Viking Lander 2 (Fig. 1) dug trenches ~15 cm deep at 48°N (*26*) and did not discover ice (the model predicts ice at 24 cm). Given our observations, it is likely that ice exists here slightly deeper than excavated to in the 1970s.

The highest-latitude ice-free craters could place an upper limit on the long-term average of atmospheric water vapor. Six new craters poleward of 30°N (and at lower latitudes than sites 1 to 5) that do not show evidence of this bright ice are known (table S1). However, ice at site 1 became unrecognizable within months, and all these craters may be up to years old, so their current ice-free appearance may not indicate a lack of the clean ice layer at these locations (further discussion in the SOM).

The origin of this clean ice is not obvious. It can be removed by diffusion to the atmosphere, but diffusion of vapor into the regolith creates only pore-filling ice. Burial of dusty snow (*27*) deposited during high obliquities (perhaps as recently as ~400,000 years ago when obliquity was 30°) has been suggested, yet simulations (*4*, *28*, *29*) indicate that buried ice at this latitude is efficiently removed during low-obliquity pe-

Table 1. Timing, locations and observations of sites 1 to 5. Martian dates are given by aerocentric longitude of the Sun (L_s) and Mars year (M29 started 12/2007). Image names beginning with V are from the Thermal Emission Imaging System visible camera; names beginning with P/B are from CTX and abbreviated (full names: P22_009556_2263_XI_46N183W, P20_008699_2247_XN_44N182W, P21_009095_2225_XN_42N195W, B01_010058_2375_XN_57N209W, B01_010018_2247_XN_44N195W, and P20_009015_2262_XI_46N171W). Crater diameters and depths (shadow measurements) are measured off the HiRISE image (denoted by an asterisk). Both ice-containing craters at site 1 were measured. There was no identifiable shadow at site 3. Rightmost column shows mean and range of predicted ice depths within a 9 km by 9 km region centered on each site (*9*).

Site	Lon. (°E)	Lat. (°N)	Latest image before impact	Earliest image after impact	HiRISE	L_s M29	Diam. (m)	Depth (m)	Model ice depth (m)
1	176.90°	46.33°	6/4/2008	8/10/2008	PSP_009978_2265	125.9	4	0.55	0.51
			L_s 81/M29	L_s 111/M29	PSP_010189_2265	133.8			(0.36–0.73)
			P20_008699_2247	P22_009556_2263	PSP_010334_2265	139.3			
					PSP_010400_2265	141.9	3.75	0.42	
					PSP_010901_2265	162.0			
					ESP_011323_2265*	180.0			
					ESP_011468_2265	186.5			
					ESP_012602_2265	240.3			
2	164.22°	43.28°	12/22/2006	7/5/2008	PSP_010084_2235	129.8	6	1.33	0.74
			L_s 154/M28	L_s 94/M29	PSP_010440_2235	143.5			(0.34–∞)
			V22273012	P21_009095_2225	PSP_010651_2235	151.8			
					ESP_011574_2235*	191.2			
					ESP_011719_2235	197.9			
					ESP_012497_2235	235.1			
3	150.62°	55.57°	1/26/2008	9/18/2008	PSP_010625_2360*	150.8	8	?	0.12
			L_s 23/M29	L_s 129/M29	ESP_011337_2360	180.7			(0.09–0.15)
			V27128013	B01_010058_2375	ESP_011548_2360	190.1			
4	164.71°	45.05°	1/22/2008	9/15/2008	PSP_010585_2255	149.2	6	1.76	0.38
			L_s 21/M29	L_s 127/M29	ESP_011442_2255*	185.3			(0.10–∞)
			V27090026	B01_010018_2247	ESP_012220_2255	221.6			
5	188.51°	46.16°	7/3/2004	6/28/2008	PSP_010861_2265	160.4	12	2.46	0.14
			L_s 55/M27	L_s 92/M29	ESP_011283_2265	178.3			(0.12–0.16)
			V11315010	P20_009015_2262	ESP_011494_2265*	187.6			
					ESP_011850_2265	204.0			

riods (obliquity was 20° ~350,000 years ago). Pure terrestrial ground ice forms quickly by thermomolecular forces (*30*) from thin films of liquid water (frost heave), and this process may extend to Mars for brines (*31*). Alternatively, thermal contraction of pore-ice and subsequent vapor deposition may build increasingly pure ground ice, but requires long times (*32*).

Small, frequent impacts combined with medium- and high-resolution imaging offer a method to gauge the depth and extent of buried ice and probe beneath the top of the ice table. The ice appears to be heterogeneously distributed with depth and includes a relatively clean layer <1 m thick where sampled. Comparing these data with model results tells us about the time-averaged atmospheric water content. The available sites support a value of 20 pr-μm (higher than today's value), indicating current ice-table retreat likely forced by recent orbital change (*4*, *28*, *29*).

References and Notes

1. R. B. Leighton, B. C. Murray, *Science* **153**, 136 (1966).
2. D. A. Paige, *Nature* **356**, 43 (1992).
3. M. T. Mellon, B. M. Jakosky, *J. Geophys. Res.* **98**, 3345 (1993).
4. M. T. Mellon, B. M. Jakosky, *J. Geophys. Res.* **100**, 11781 (1995).
5. W. V. Boynton *et al.*, *Science* **297**, 81 (2002).
6. W. C. Feldman *et al.*, *Science* **297**, 75 (2002).
7. I. Mitrofanov *et al.*, *Science* **297**, 78 (2002).
8. W. C. Feldman *et al.*, *J. Geophys. Res.* **109**, E09006 (2004).
9. M. T. Mellon *et al.*, *Icarus* **169**, 324 (2004).
10. M. E. Smith, *Icarus* **167**, 148 (2004).
11. T. Fouchet *et al.*, *Icarus* **190**, 32 (2007).
12. NS results are model dependent, have an effective resolution of only ~600 km, and are complicated by spatial heterogeneity and soil chemistry uncertainties (*33*). The NS is also insensitive to ice buried by a few decimeters (pure ice buried by 40 to 60 g cm^{-2} appears to have equatorial hydrogen abundances).
13. Centimeters of ice effectively thermalizes neutrons, rendering the NS insensitive to deeper changes in ice concentration (*34*).
14. M. C. Malin *et al.*, *Science* **314**, 1573 (2006).
15. M. C. Malin *et al.*, *J. Geophys. Res.* **112**, E05S04 (2007).
16. HiRISE acquires images in three bands (550, 700, and 900 nm) with pixel scales of 25 to 32 cm (*35*).
17. S. Murchie *et al.*, *J. Geophys. Res.* **112**, E05S03 (2007).
18. B. A. Cantor, *Icarus* **186**, 60 (2007).
19. S. W. Squyres, M. H. Carr, *Science* **231**, 249 (1986).
20. J. W. Holt *et al.*, *Science* **322**, 1235 (2008).
21. J. J. Plaut *et al.*, *Geophys. Res. Lett.* **36**, L02203 (2009).
22. E. M. Fischer, C. M. Pieters, *Icarus* **102**, 185 (1993).
23. H. H. Kieffer, *J. Geophys. Res.* **95**, 1481 (1990).
24. P. H. Smith *et al.*, *Science* **325**, 58 (2009).
25. M. T. Mellon *et al.*, *Lunar Planet. Sci. Conf.* **40**, 1904 (2009).
26. H. J. Moore *et al.*, *J. Geophys. Res.* **84**, 8365 (1979).
27. J. F. Mustard, C. D. Cooper, M. K. Rifkin, *Nature* **412**, 411 (2001).
28. M. A. Chamberlain, W. V. Boynton, *J. Geophys. Res.* **112**, E06009 (2007).
29. N. Schorghofer, *Nature* **449**, 192 (2007).
30. A. W. Rempel, J. S. Wettlaufer, M. Grae Worster, *J. Fluid Mech.* **498**, 227 (2004).
31. R. D. Miller, P. B. Black, *J. Geophys. Res.* **108**, 8041 (2003).
32. D. A. Fisher *et al.*, *Icarus* **179**, 387 (2005).
33. B. Diez *et al.*, *Icarus* **196**, 409 (2008).
34. W. C. Feldman *et al.*, *J. Geophys. Res.* **98**, 20885 (1993).
35. A. S. McEwen *et al.*, *J. Geophys. Res.* **112**, E05S02 (2007).

36. Funding for this work was provided by the NASA Mars Reconnaissance Orbiter (MRO) project. We thank the CTX, HiRISE, CRISM, and MRO-operations teams for the (time-critical) acquisition of these data and three reviewers for their helpful comments.

Supporting Online Material
www.sciencemag.org/cgi/content/full/325/5948/1674/DC1
SOM Text
Figs. S1 to S4
Table S1
References

22 April 2009; accepted 28 July 2009
10.1126/science.1175307

www.sciencemag.org/cgi/content/full/325/5948/1674/DC1

Supporting Online Material for

Distribution of Mid-Latitude Ground Ice on Mars from New Impact Craters

Shane Byrne,* Colin M. Dundas, Megan R. Kennedy, Michael T. Mellon, Alfred S. McEwen, Selby C. Cull, Ingrid J. Daubar, David E. Shean, Kimberly D. Seelos, Scott L. Murchie, Bruce A. Cantor, Raymond E. Arvidson, Kenneth S. Edgett, Andreas Reufer, Nicolas Thomas, Tanya N. Harrison, Liliya V. Posiolova, Frank P. Seelos

*To whom correspondence should be addressed. E-mail: shane@lpl.arizona.edu

Published 25 September 2009, *Science* **325**, 1674 (2009)
DOI: 10.1126/science.1175307

This PDF file includes:

Materials and Methods
SOM Text
Figs. S1 to S4
Tables S1
References

Distribution of Mid-Latitude Ground-Ice on Mars from New Impact Craters

Supplementary Online Material

Detection of New Impacts

New impacts are most easily detected where the impact can disturb surficial dust and darken the surface (S1). CTX panchromatic images (pixel scales of 5-6m) are examined by the CTX science team for evidence of recent impacts i.e. dark patches in otherwise bright areas (Fig. S1). When earlier images differ in appearance, HiRISE data are acquired to confirm an impact origin and measure crater diameter. Over 80, unevenly distributed, new impact craters have been confirmed in this way. These discoveries are biased to dust covered regions of Mars that commonly have clear atmospheric conditions during spring and summer. The bias toward dust-mantled regions results from the formation of dark ejecta and disrupted surfaces during the impact event; less-dusty surfaces do not show sufficiently large “blast zones” to render craters of less than about 20–25 m diameter visible in 6 m/pixel images.

The acquisition dates of image pairs like that shown for site 1 in Fig. S1 provide constraints on the time of the impact. Table 1 lists these constraints for the five sites discussed in this paper. Most were less than a few months old when discovered. Sites 2 and 5 could be much older; however, given the rates at which this icy material is changing (Fig. S2), they also likely formed during 2008. These impacts are likely to have a spread of ages as their spatial distribution would be difficult to explain as a single event; however, there are no data to rule out the possibility that they all formed nearly simultaneously in a single meteor shower between June 4th and June 28th in 2008.

Although these craters are typically much smaller than the dark disturbed region that surrounds them, ice deposits at sites 3 and 5 were extensive enough to be visible in CTX images (Fig. S1).

Regional context of sites 1-5

Figure S1 shows regional views centered on each impact site. In general these are all young terrains with few superposed craters.

Sites 3 and 5 are topographically flat. Site 3 is located on dark plains within Vastitas Borealis thought to be composed of outflow channel sediments reworked by periglacial processes (S2). Numerous dust devil tracks cover this area. Site 5 is located within Amazonis Planitia on deposits of early to middle Amazonian age that emanate as flows from Olympus Mons (S2). Pervasive polygons here and at site 1 attest to the recent presence of ground ice.

Sites 1,2 and 4 occur in more rugged terrain. Sites 2 and 4 occur in the Phlegra Montes, part of the late-Noachian/early-Hesperian Nephenthes Mensae unit that is composed of eroded knobs of highland rock with associated debris-covered aprons (S2). Site 2 certainly occurs on one of these lobate aprons (emanating from the massif to the east, see Fig. S1). Site 4 occurs in an area where several of these aprons may have coalesced and shares the same characteristic surface texture as site 2. Site 1 occurs near the edge of one of these aprons (emanating from a nearly-buried massif to the south, see Fig. S1). It is not immediately clear whether it is representative of one of these lobate aprons or the surrounding terrain (which, as with, site 3 is interpreted as periglacially reworked outflow channel sediment).

Observed changes at sites 2-5

Table 1 details our HiRISE observations for sites 1-5. All sites showed evidence of change both in the area that was ice covered (which shrank) and the brightness and color of the remaining ice (which decreased and reddened). Site 1 ice decreased in brightness but did not shrink in area. Evidence for these changes at site 1 was presented in Fig. 2 of the main article and evidence of these changes for sites 2-5 is shown here in Fig. S2. Each color band of the HiRISE data shown in Figs. 2 and S2 is ratioed to the mean brightness in that band of an undisturbed region (256mx256m) roughly one kilometer south of the impact site. The exact position of these reference regions was shifted to avoid large topographic features that have a slope-induced brightness uncharacteristic of the surface material such as rims of nearby large craters. Thus, ignoring the contrast reduction due to atmospheric dust, color and brightness in the sub-frames of Figs. 2 and S2 can be compared at each site. This correction applies only to illuminated terrain. As the incidence angle increases small-scale roughness causes shadows to lengthen and appear (which gives an overall darkening appearance). When examining the trend of the terrain brightness around the craters we pick areas that have no visible shadows.

The common behavior of these sublimating ice patches is a sharp reduction of their reflectance in the blue-green channel with more modest changes in the red and near-infrared channels. The dark 'blast zones' around the craters brighten somewhat (e.g. site 1), or remain unchanged during the observational period.

CRISM Data Preparation

To remove the effects of atmosphere and aerosol absorptions, scatterings, and emissions, CRISM spectra were modeled with the Discrete Ordinate Radiative Transfer (DISORT) code of (S3) which has been adapted for use with CRISM images (S4). DISORT models the reflectance that CRISM would measure if looking through a Mars-like atmosphere at a surface that scatters light according to the Hapke model (S5). The code treats the atmosphere as parallel layers composed of CO, CO_2, and H_2O vapor, and requires inputs of historical climatological data (S6-S8).

Several DISORT runs were conducted with various single-scattering albedos, and the relationship between single-scattering albedo and observed I/F was fit using a fifth-order polynomial. A look-up table was then used to convert the CRISM I/F data to single-scattering albedo.

Thermal model description

The reader is referred to Dundas et al. (currently submitted to Icarus) for a full description of the model. A summarized description follows here.

The thermal model developed and used here is a one-dimensional explicit solution of the heat diffusion equation in the martian subsurface where boundary conditions are incoming solar flux, downwelling long-wavelength atmospheric radiation (set to 4% of the noontime short-wave flux) and thermal emission at the surface and constant planetary heat flow of $30 mWm^{-2}$ at the base of the model domain. The thickness of numerical layers in the subsurface is chosen so that the diurnal temperature wave is resolved by at least 10 layers (thicknesses also increase with depth by a constant factor for computational efficiency) and the model extends to depths sufficient to capture the annual thermal wave. Time increments in the model are chosen in conjunction with the layer thicknesses and material thermophysical properties to satisfy the Courant criterion for numerical stability. The model is divided into three material layers. A ground ice layer of adjustable thickness and depth is sandwiched between two dry regolith layers that extend from the ice to the surface and bottom of the model domain respectively. The model includes the effects of seasonal CO_2 frost formation, although this frost does not form at every site. We assume a flat surface with no radiative contribution from nearby slopes (which will cause an eventual underestimate of total sublimation) although shadowing by the crater walls at site 1 is accounted for.

We used a thermal inertia typical of the impact site area (S9) to estimate the thermal conductivity of the original overlying regolith, assuming the same density and heat capacity as (S10), and the measured albedo from the Thermal Emission Spectrometer (TES) (S11). We varied the initial albedo of the ice and forced it to decrease linearly with time to the ice-free condition we observed in the later HiRISE data, which is actually a little darker than the pre-impact dust-covered terrain (see Figs. 2 and S2).

This model was run for sufficient time (usually several decades) to stabilize the temperature profile to serve as the pre-impact initial condition. In our nominal case, we assumed pure ice buried beneath 0.5m of regolith. At the time of impact, we remove the overlying dry soil and run the model forward in time to track the temperature of the exposed ice. We experimented with adding heat due to the impact in the form of artificially boosting the initial temperature of the exposed ice. Ignoring this extra heat means that the total sublimations quoted below are again slightly underestimated. During the remainder of the model run we track the thinning of the uppermost ice layer when figuring surface temperature and the cooling effect of latent heat of sublimation. We also continued to model the temperature of the pre-impact surface as a proxy for the regional temperature. The atmospheric temperature was estimated from this regional surface temperature in a way that ensured it was close to equal at night, but was approximately 20-25K lower during the day, consistent with Viking Lander 2 measurements (S12). Although our model is one-dimensional we included an estimate of the effects of lateral heat conduction from ice exposed on the crater floor to adjacent buried ice. We calculated conductive losses through the edge of the exposed ice patch at every depth using both temperatures of the exposed and buried ice and the heat-diffusion length scale, which increases as the square-root of time. This effect served to reduce the temperature of the exposed ice and lowered the total sublimation calculated by roughly 40% (the exact amount depends on other model parameters).

For simplicity, we assumed a constant near-surface water vapor partial pressure (unless this resulted in the atmosphere being saturated. In that case it was held at the saturation pressure) estimated from the column abundance and condensation height of (S6). This abundance may be an overestimate (S13) and also neglects a seasonal decrease in late summer. These approximations again result in a conservative estimate of sublimation, as lower humidity will increase ice loss. Sublimation was calculated using equations for free and forced convection based largely on those used for previous studies. (e.g. S14-S16). The formulae we used (S17) differ in two small ways, which produce more complex behavior but in most cases have the combined effect of again reducing the total sublimation we calculated by less than a factor of two. The more significant of these two changes involved including temperature when calculating the density difference between the saturated boundary layer and surrounding atmosphere (the $\Delta\rho/\rho$ term of S14-S16). Previous studies calculated this difference based only on the different mean molecular weights and assumed that the boundary layer and atmosphere were isothermal. Forced convection depends on the product of the drag coefficient and wind speed; we varied a constant windspeed to investigate this. We took the typical windspeed to be 2.5 m/s, similar to that at the Viking 2 landing site (S12). The model was run forward in time until L_s 171° (the mid-point of the last image containing ice and the first image with no visible sign of ice) at which point the total amount of sublimation is output.

We varied several parameters including the date of impact, the depth and thickness of the ice layer, the initial albedo of the ice, the wind speed, the thermophysical properties of the surrounding landscape and pre-impact terrain and the degree of coupling between the atmospheric and regional surface temperatures. In our nominal case, the time of impact was L_s 96° (the mid-point of the allowed range), the ice was assumed to lie 0.5m below the surface (the current depth of the exposed ice), the initial albedo of exposed ice was set to 0.4, wind speed was 2.5 ms^{-1} and pre-impact surface albedo and thermal inertia were taken from the TES results (S9, S11). The parameters most influential on the total sublimation were windspeed (investigated range of 0-7.5 ms^{-1}) and the initial ice albedo (investigated range of 0.3-0.5).

Varying these parameters within reasonable ranges yielded total sublimations of between 0.3-6.5mm, with our nominal case yielding 1.7mm of total sublimation. At each step in this process choices were made that would consistently underestimate the total ice sublimation. We therefore consider millimeters of sublimation to be a robust lower limit. This underestimation is intentional as higher sublimation would reinforce our main conclusion that the sublimating ice we observe is clean.

Currently Ice-Free High-Latitude Craters

Table S1 details fresh impact craters at latitudes poleward of ±30° that show no evidence for a clean ice layer in HiRISE data. All these craters may be up to a few years old so their current ice-free appearance may not indicate a lack of sub-surface ice at these locations. Of these currently ice-free craters, only one is known with certainty to have formed less than a year before being imaged by HiRISE (site 11, about 400km south of site 5). It is possible that a clean layer of buried ice is not present at this lower latitude (39.6°N) or the excavation depth was insufficient to expose it, however the impact occurred a minimum of 71 days before the initial HiRISE followup image (and possibly up to a year before) so excavated ice may also have sublimated enough to be hidden by a lag deposit as observed at site 1.

Some of these sites have morphologic indicators that suggest ice may once have been present. For example, a cluster of craters at site 12 contains individual craters with flat floors a few decimeters deep that are very similar to those at site 1 in appearance and dimensions (Fig. S3). Craters in this cluster obviously excavated down to a resistant material that has a depth consistent with ground ice. Sites 9 and 12 are likely to host sub-surface water ice on the basis of the same modeling that successfully explains the five icy sites described in the main text

(S8). Sites 6 and 7 in the southern hemisphere are likewise expected to host stable ground ice.

The southern hemisphere is underrepresented in our sample of high-latitude craters for a number of reasons. The current argument of perihelion causes aphelion to occur in the northern summer. When Mars is closer to the asteroid belt the impact rate is higher. Up to six or seven times more craters are expected to form at aphelion (near northern summer solstice) than perihelion (near southern summer solstice) (S18). As time is critical in detecting ice at these sites before it fades away and most imaging occurs in late spring and early summer due to favorable lighting we should expect to discover ice at more of these sites in the northern hemisphere. Another important factor discussed earlier is the presence of large expanses of dusty areas in the northern hemisphere (enabling these impacts to be discovered) which the southern hemisphere lacks (S19). The two high-latitude southern-hemisphere impacts discovered (sites 6 and 7, Table S1) occur in the Argyre and Hellas basins respectively, which are moderately dusty (S19). These basins may yield more impact discoveries in subsequent southern summers; however, their surfaces are also frequency obscured by clouds and dust storms.

Model Predictions of Mid-Latitude Ice Table Depths

The mid-latitude locations of these craters make them especially valuable for validating previous models. The depth to stable ground ice is expected to increase with decreasing latitude in a very sensitive manner in this zone (Fig. S4). A sharp latitudinal cutoff where ice is no longer stable at any depth occurs in this mid-latitude zone. This cutoff is a salient feature of all recent models of ground-ice stability (e.g. S10, S20, S21) and its position has been shown to be sensitive to variation in the long-term average atmospheric water vapor.

Comparison of crater depths (an upper limit on excavation depth due to downward deflection of the substrate during impact) with expected ice table depth shows that all these sites are consistent with model predictions (S10) when 20pr-μm of atmospheric water vapor is used. Usefully, some of these sites can be seen (Fig. S4) to be on the edge of the region where ice is expected which rules out atmospheric water vapor concentrations of less than 20pr-μm. As discussed in the previous section, craters equatorward of this area do not show evidence of this bright ice layer. However, due to their possible age, ice may still exist there underneath a sublimation lag so these data could also be consistent with a long-term average atmospheric vapor concentration even greater than 20pr-μm (although the coincidence of the expected ice depth with crater depth at site1 argues for a value close to 20pr-μm).

Models that attempt to couple changing orbital elements with atmospheric water vapor (e.g. S21) predict that this ice-stability boundary can vary by several degrees of latitude over recent time. The model of Chamberlain and Boynton (S21) suggests that variations in the argument of perihelion over the past 10 Kyr alone would have caused this boundary to shift by 10-15 degrees of latitude in the northern hemisphere. Thus, accurately constraining the position of this boundary from observations of these newly formed craters is a great opportunity to understand the history of ground ice and atmospheric water vapor on Mars.

Supplementary Online Material References

S1. M.C. Malin et al., *Science*, **314**, 1573-1577(2006).

S2. K.L. Tanaka, J.A. Skinner, T.M. Hare, *U.S.G.S. Map*. **2888** (2005).

S3. K. Stamnes et al., *Appl. Optics*, **27**, 2502-2509 (1988).

S4. R.E. Arvidson et al., *AGU Fall meeting*, **P33C-01** (2008).

S5. B. Hapke, Theory of reflectance and emittance spectroscopy, Cambridge University Press (1993).

S6. M.E. Smith, *Icarus*, **157**, 259-263,(2002).

S7. B.J. Conrath et al., *J. Geophys. Res.*, **105**, 9509-9520 (2000).

S8. M.E. Smith, *Icarus*, **167**, 148-165, (2004).

S9. N.E. Putzig et al., *Icarus*, **191**, 68-94 (2007).

S10. M.T. Mellon et al., *Icarus*. **169**, 324-340 (2004).

S11. P.R. Christensen et al., *J. Geophys. Res.,* **106**, 23823-23872 (2001).

S12. S.L. Hess et al., *J. Geophys. Res.*, **82**, 4559-4574, (1977).

S13. T. Fouchet et al., *Icarus*, **190**, 32-49 (2007).

S14. A.P. Ingersoll, *Science*, **168**, 972-973 (1970).

S15. A.B. Ivanov and D.O. Muhleman, *Icarus*, **144**, 436-448 (2000).

S16. K.E. Williams et al., *Icarus*, **196**, 565-577 (2008).

S17. A.F. Mills, *Mass Transfer*, p53-54, Prentice Hall, NJ, (2001).

S18. B.A. Ivanov, *Space Sci. Rev.,* **96**, 87-104 (2001).

S19. S.W. Ruff and P.R. Christensen, *J. Geophys. Res.*, **107**, E12 (2002).

S20. N. Schorghofer and O. Aharonson, *J. Geophys. Res*., **110**, E05003 (2005).

S21. M.A. Chamberlain and W.V. Boynton, *J. Geophys. Res*., **112**, E06009 (2007).

Supplementary Online Material Figure Legends

Figure S1.

CTX images of the regional context centered on each impact site (see Fig. 1 and Table 1 for image names and locations). Insets in the top-right of each panel are 1km across. Top panels show the CTX image pair that led to the discovery of the site 1 impact; other panels show post-impact views of sites 2-5. All panels have north at top and are illuminated from the lower-left.

Figure S2.

HiRISE false color data (see Fig. 1 and Table 1 for locations, dates and image names) showing ice patches and their sublimation at sites 2-5. The panels are 35m across, have north at the top and are illuminated from the lower left. The plots on the right show the brightness evolution of an icy patch (solid) and dark impact zone (dashed) in the three HiRISE filters scaled by the brightness of the surrounding undisturbed terrain (to remove incidence angle and first order atmospheric effects).

Figure S3.

HiRISE false color data (see Tables 1 and S1 for locations, dates and image names) showing currently ice-free craters at sites 1 (top) and 12 (bottom). The panels are 20m across, have north at the top and are illuminated from the lower left.

Figure S4.

Depths to stable ground ice as a function of latitude (S10) for sites 1-5 and Viking Lander 2. Crater locations are indicated by vertical dashed lines while crater depths are indicated by horizontal dashed lines. No reliable crater depth could be measured for site 3. Line intersections show that sites 1-5 are expected to have excavated to ground ice whereas Viking Lander 2 missed discovering ground ice by 10cm.

Table S1.

Timing, locations and observations of the eight impact sites with latitude poleward of 30° that were not observed to contain bright ice. Image names starting with H were acquired by the High-Resolution Stereo Camera on Mars Express, beginning with M were acquired by the Mars Orbiter Camera and beginning with I by the THEMIS IR camera. Full names of CTX images are P14_006704_1279_XI_52S053W, P15_006739_1314_XN_48S290W, P21_009144_2133_XN_33N092W, P17_007735_2186_XN_38N137W, B02_010505_2205_XN_40N170W, P20_009027_2190_XN_39N138W and P17_007514_2208_XN_40N223W.

	Lon.	Lat.	Latest Before	Soonest After	HiRISE	L_s/M29
6	305.99°	-50.60°	1/31/2006 L_s 5/M27 V18325004	12/31/2007 L_s 11/M29 P14_006704_1279	PSP_007561_1290	41.8
7	70.10°	-50.16°	11/26/2005 L_s 330/M27 I17522007	1/3/2008 L_s 12/M29 P15_006739_1314	PSP_007596_1295	43.1
8	268.117°	33.15°	4/20/2005 L_s 196/M27 H1616_0000_ND3	7/9/2008 L_s 96/M29 P21_009144_2133	PSP_010634_2135	151.1
9	222.27°	37.46°	12/20/2006 L_s 153/M27 V22246010	3/21/2008 L_s 48/M29 P17_007735_2186	PSP_008236_2180	65.1
10	123.72°	38.92°	6/15/1999 L_s 155/M24 M02-02002	12/25/2007 L_s 8/M29 V26742021	PSP_010547_2195	147.7
11	190.04°	39.55°	12/10/2007 L_s 1/M29 V26565016	10/23/2008 L_s 146/M29 B02_010505_2205	ESP_011428_2200	184.7
12	221.22°	40.31°	2/6/2005 L_s 156/M27 V13972003	6/29/2008 L_s 92/M29 P20_009027_2190	ESP_011295_2205	178.8
13	136.58°	40.35°	4/24/2005 L_s 199/M27 H1632_0000_ND3	3/3/2008 L_s 40/M29 P17_007514_2208	PSP_008015_2205	57.5

Table S1

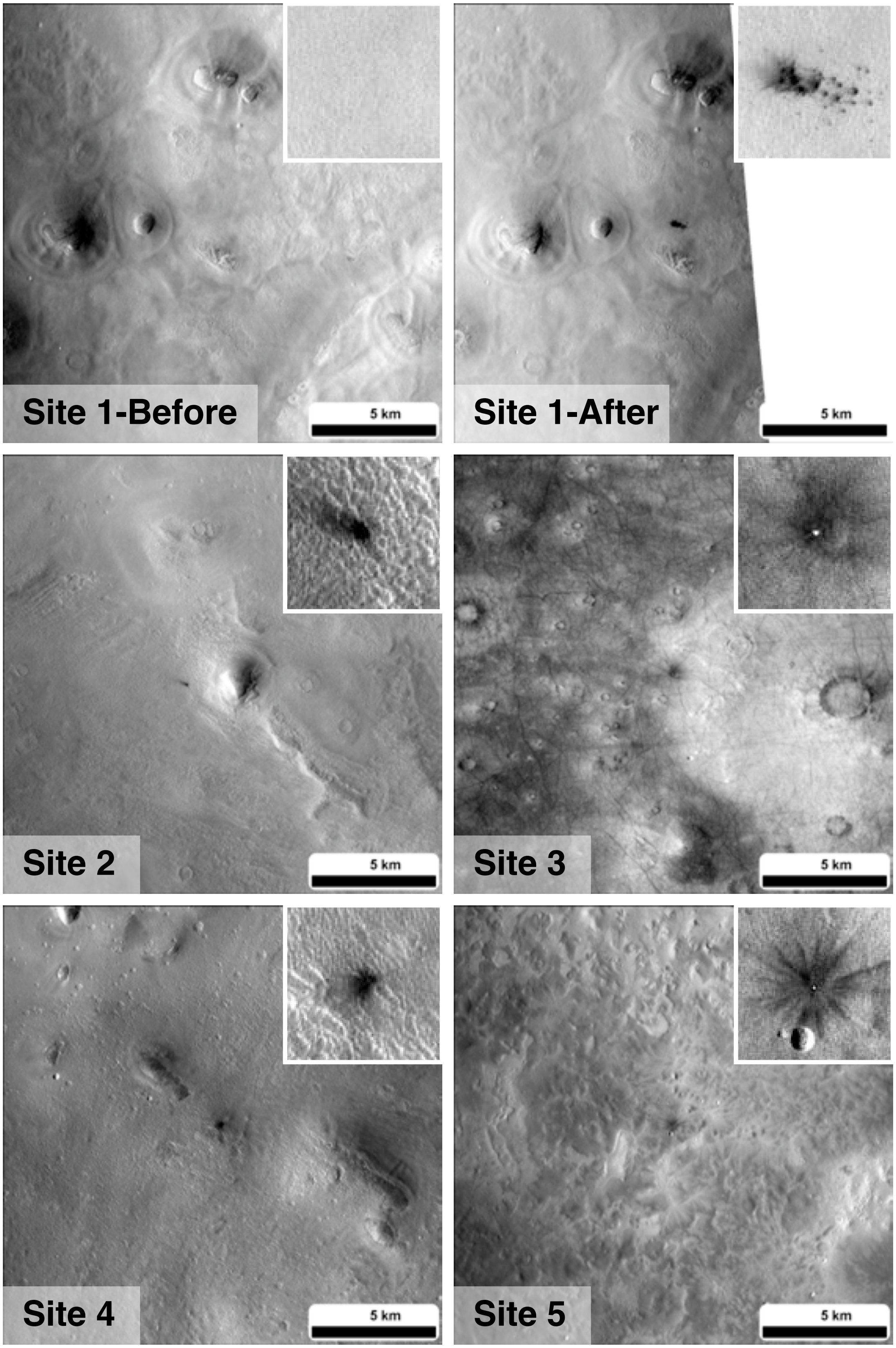
Site 1-Before
5 km
Site 1-After
5 km
Site 2
5 km
Site 3
5 km
Site 4
5 km
Site 5
5 km

Figure S1

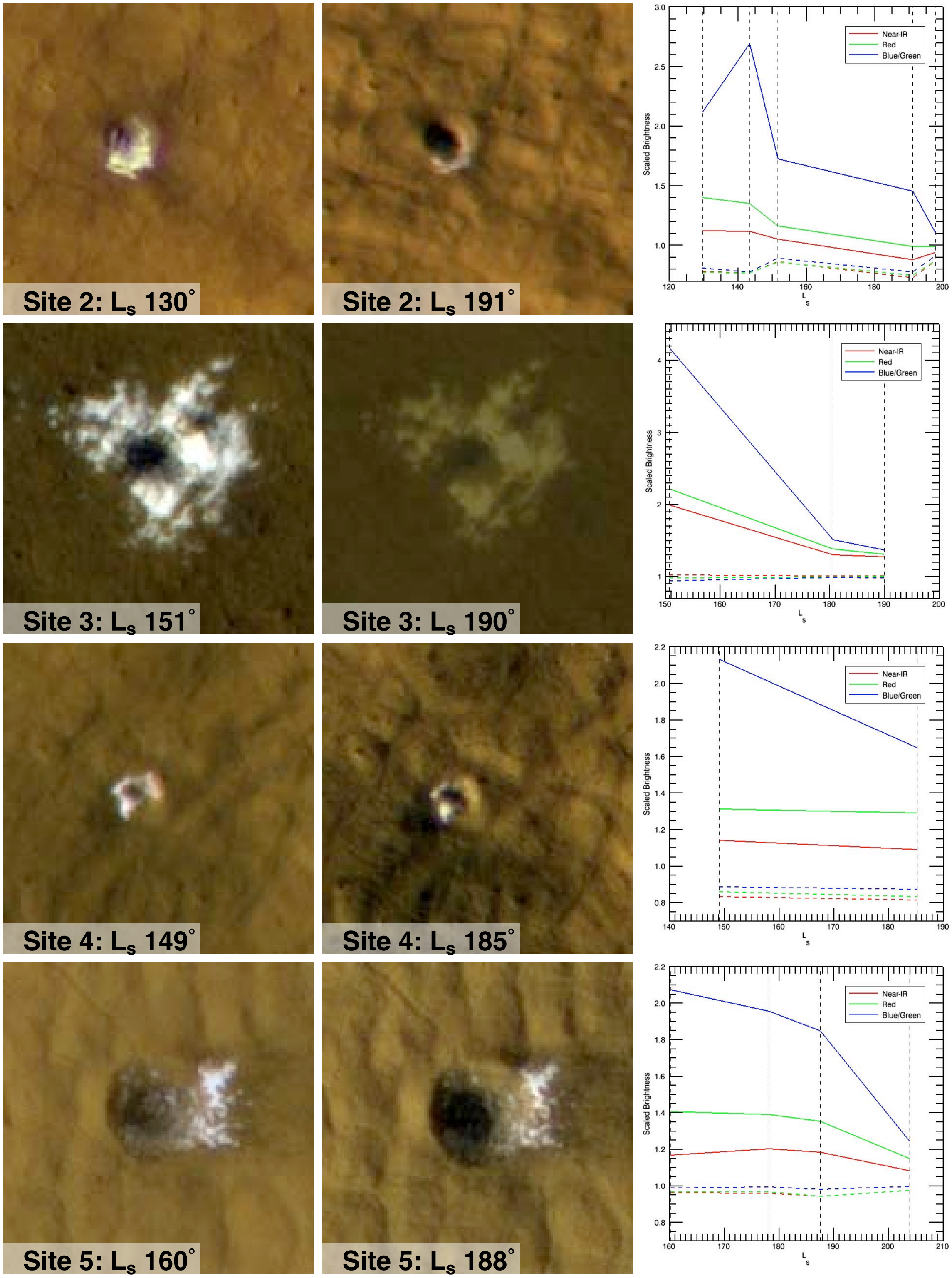

Site 2: Ls 130°
Site 2: Ls 191°
Site 3: Ls 151°
Site 3: Ls 190°
Site 4: Ls 149°
Site 4: Ls 185°
Site 5: Ls 160°
Site 5: Ls 188°
Near-IR
Red
Blue/Green
Scaled Brightness
Ls

Figure S2

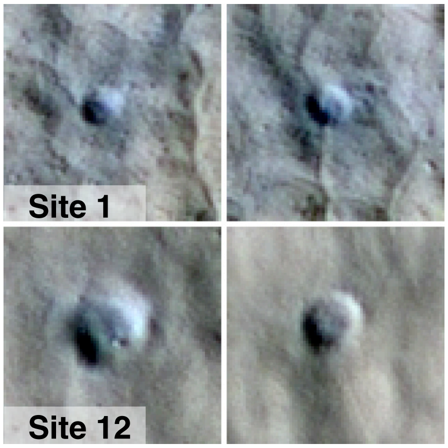

Figure S3

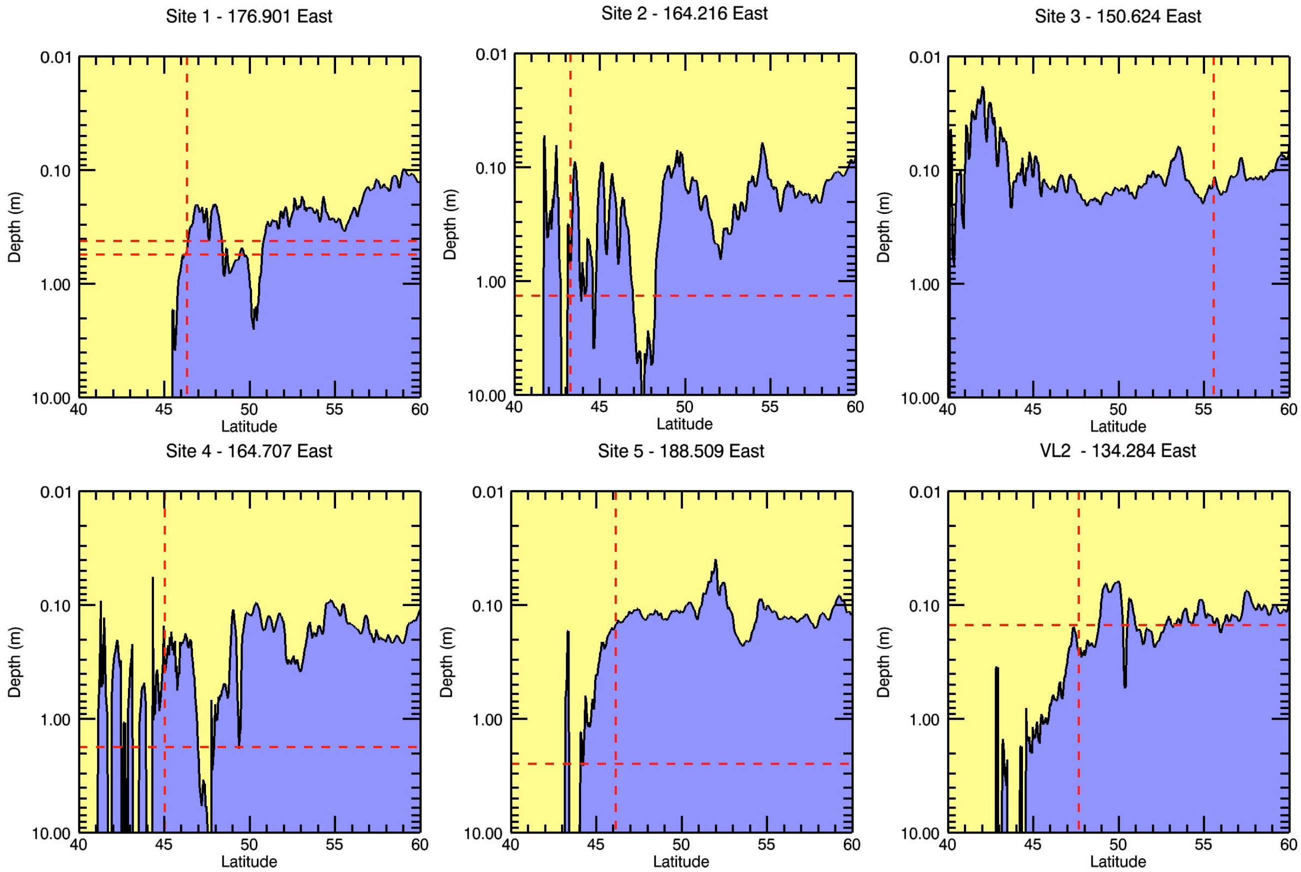

Site 1 - 176.901 East
Site 2 - 164.216 East
Site 3 - 150.624 East
Site 4 - 164.707 East
Site 5 - 188.509 East
VL2 - 134.284 East
Depth (m)
Latitude
0.01
0.10
1.00
10.00
40
45
50
55
60

Figure S4